Three-dimensional gas-liquid flow simulation of a rotating packed bed using Eulerian porous media models

Hui Han*[1,2], Jiangshuai Yan[1,2], Yuxing Li[1,2], Jianlu Zhu[1,2], Nan Li[1,2]

[1]*College of Pipeline and Civil Engineering, China University of Petroleum (East China), Qingdao, Shandong 266580, China*

[2] *Shandong Provincial Key Laboratory of Oil and Gas Storage and Transportation Security, China University of Petroleum (East China), Qingdao, Shandong 266580, China*

Corresponding author. Tel: (+86) 532 8698 1818; fax: (+86) 29 8266 5445

Email address: hanhui@upc.edu.cn

Abstract

The rotating packed bed (RPB) is a typical equipment in chemical process intensification technology due to its excellent mass transfer performance. In this paper, a three-dimensional full-scale model was established based on the Eulerian two-fluid method to study the gas-liquid two-phase flow in RPBs. Three different single-phase wire screen packing pressure drop models coupled with the interfacial area model were used to construct resistance calculation methods for porous media, respectively. The results show that the porous media resistance models based on diverse single-phase models can accurately simulate the flows of gas and liquid in the RPB packing under different conditions, where simulation deviations of the liquid holdup and the pressure drop of the m-K model range from 0.92% to 27.61% and 1.63% to 34.59%, respectively. In addition, the simulation accuracy of the liquid holdup of three models was obviously influenced by the rotational speed (*N*). The m-K model has the highest prediction accuracy at *N*=500~1500 rpm. At *N*=2000~2500 rpm, the B model has the highest prediction accuracy. The higher the viscosity of the liquid, the more uniform the axial liquid distribution in the packing, and the longer the liquid mean residence time. As the viscosity of the liquid increases from 1.003mPa•s to 155.6mPa•s, the mean residence time range of the liquid significantly increases from 0.0576 to 0.1686 s to 0.0991 to 0.3678 s. The impact of different nozzle designs on liquid distribution has been investigated using a new method based on user-defined functions (UDFs). A more homogeneous distribution of liquid within the packing can be achieved by increasing nozzle height, decreasing nozzle size, and increasing the number of nozzles.

Keywords: gas-liquid flow; Eulerian approach; porous media; rotating packed bed; nozzle design

1. Introduction

Process intensification as a smaller, cleaner, safer, and more energy-efficient technology is an effective means of reducing environmental effects in the chemical production [1]. As a representative equipment for process intensification, the Rotating Packed Bed (RPB) is characterized by high mass transfer efficiency, small size, light weight, low energy consumption, good

operational flexibility, and ease of scale-up [2,3], which make RPBs uniquely advantageous for mass transfer limited reactions and combinations of several unit operations in one apparatus [3]. Currently, RPBs are widely applied for process intensification of various reactions and separations such as organic pollutants degradation [4], catalyst preparation and application [5,6], wastewater treatment [7], wet dust removal and purification [8,9], and acid gas removal [10-13]. The mass transfer characteristics between gas and liquid phases in RPBs, while serving as the basis for reactor design, are unanimously considered to be strongly dependent on the flow behavior of fluid. Therefore, the study of hydrodynamic characteristics is extremely important for the RPB analysis, which provides a scientific basis for explaining the mechanism of mass transfer enhancement in RPBs and thus can provide technical guidance for reactor design optimization in different applications.

The hydrodynamic characteristics in RPBs have been studied extensively by many scholars so far. Due to the nonlinear flow in RPBs, theoretical analysis method cannot give an analytical solution [14]. Therefore, researches on the hydrodynamic characteristics of RPBs have mainly focused on two aspects: experimental researches and computational fluid dynamics (CFD) simulation researches. High-speed camera technology [15-19] and computed tomography (CT) technology [20,21] as non-intrusive imaging techniques have been extensively used to obtain the flow patterns and distribution of liquid within RPBs since the 2110s. In addition, colored fluid tracing [22] and dye adsorption [21] have been used to obtain the trajectory of liquid movement and wetting efficiency in RPBs, respectively. Although the above experimental methods can visually help us to obtain fluid flow information inside RPBs, there are still some basic data that are difficult to acquire owing to the intricate structure of RPBs. For instance, under varying operational conditions, it is difficult to acquire information such as fluid velocity, concentration gradient, turbulent energy, and instantaneous drag force [14,23]. In recent years, as the swift progress of computer-related technologies, CFD methods have gradually become an effective tool for studying flow, mass transfer, reaction and structural optimization. CFD methods are easily available for obtaining hydrodynamic parameters in RPBs while helping to scale RPBs from laboratory to pilot or industrial scale.

Currently, the majority of CFD models on RPBs have been developed using the commercial software Ansys Fluent. In addition, Rabiee R et al. [24] also firstly developed a model to characterize the gas-liquid flow behavior of RPBs with the aid of OpenFOAM, an open-source CFD tool. Among these CFD models, the VOF approach and Eulerian approach are two common CFD simulation methods. Since the VOF approach only deals with the control equations of a mixed phase without accounting for the momentum and mass transfers among phases, it becomes necessary to generate precise meshes and setting small time steps for the purpose of capturing the interfacial region of phases. Therefore, it will cause a significant consumption of computational resources and time while simulating the detailed liquid flow information [23,25-28], micro-mixing [29], and mass transfer [30,31] in RPBs using the VOF approach. For example, the 2D RPB simulation research carried out by Guo et al. [29] required the creation of a model with meshes count exceeding 1.4 million and the average time to compute each simulation was

more than 60 hours. Zhang et al. [28] constructed a 3D sector model for the packing with a 45° circle angle. The model simulated the packing's inner diameter, outer diameter, and height to be 19 mm, 32.75 mm, and 5.12 mm, respectively, as well as a mesh count of up to 15,261,362. Due to these drawbacks, the VOF model is difficult to be applied on pilot and industrial scale [32]. Contrarily, the Eulerian approach does not need to trace the phase interface, requires less computational grid, and has shorter computational time. For example, in the 3D full-scale flow simulation work of Zhang et al. [33], the simulated filler inner diameter, outer diameter, and height were 21, 41, and 10 mm, respectively, and the number of meshes of the model was only 51,000, which required only 0.5~3 hours to complete the calculation of a case under different working conditions. Based on these considerations, the Eulerian approach stands out as an effective and promising method for simulating gas-liquid flow and mass transfer of RPBs at both pilot and industrial scales.

Most of the CFD simulation researches of RPBs using Eulerian approach [32-36] simulated the packing as porous media through the Eulerian two-fluid model. Besides, Zhang et al. [37] also proposed to simulate the packing as solid-phase fluid and established the Eulerian three-fluid model based on this assumption. However, achieving accurate predictions of flow characteristics using either the Eulerian three-fluid or the porous media Eulerian two-fluid models critically depends on the resistance model employed to describe interphase forces. Since RPBs have different packing materials, structures, and flow characteristics compared to conventional packed beds and trickle beds, the traditional resistance models [38-40] are no longer applicable to the RPB CFD simulation researches. Kołodziej et al. [41] developed a single-phase pressure drop model applicable to the wire mesh packing, which is used as the high-porosity packing material in RPBs. Lu et al. [32,34] combined the Eulerian two-fluid method with this pressure drop model to propose a two-phase porous media resistance model of RPBs. The 2D axisymmetric CFD model was established to simulate the characteristic of gas and liquid flow [34] as well as CO_2 absorption [32] in RPBs. The simulation results proved the effectiveness of the resistance model. With reference to the Kołodziej single-phase pressure drop model [41] and its two improved models [42,43], Zhang et al. [37] utilized the Eulerian three-fluid approach to develop three novel resistance models for gas-liquid-solid systems, which were eventually applied to establish a 2D CFD model for RPBs, and subsequently evaluated and compared the accuracy of these three models. In response to the limitations of the 2D model in depicting the heterogeneous distribution of liquid in RPBs, Zhang et al. [33] upgraded the physical model to a 3D full-scale model, and verified that the resistance model was still valid for the 3D simulation.

There are two main problems in the current RPB simulation of the Eulerian approach. On the one hand, Eulerian three-fluid model is to simulate the rotation speed of the packing in the RPB by setting the solid phase to rotate at different angle velocities, which requires considering the relationship between the interfacial area of three phases, and correcting for the wettability coefficient in the three-phase drag model [37]. However, in the current reports of the interfacial area between the solid phase and gas or liquid phase, only the quantitative relationship among the gas-liquid-solid interfacial area under specific working conditions

is given, which will bring difficulties to the continued extension of this model. Contrarily, the Eulerian two-fluid model of porous media decomposes the gas-solid and liquid-solid flow resistance losses into inertial resistance losses and viscous resistance losses, which will only need to consider the interfacial area between the gas and liquid phases. On the other hand, in the 2D and 3D Eulerian two-fluid models of porous media by Lu et al. [32,34] and Zhang et al. [33], there is a lack of accuracy comparison of the porous media models. To ensure a more accurate 3D full-scale simulation of RPBs, it is essential to create corresponding three-dimensional models, followed by rigorous testing and comparative analysis of the accuracy of all models.

In this paper, a 3D full-scale model was built to simulate the gas-liquid flow in RPBs using Eulerian porous media approach. Three porous media resistance models were established based on different single-phase pressure drop models [41-43]. The effectiveness of three models in 3D dimension was verified and the simulation accuracy was compared by combining the experimental data of liquid holdup in Yang's work [20] as well as the empirical correlation of the Lashkarbolooki generic pressure drop model [44]. The comparison of model accuracy can provide a basis for selecting resistance models for simulating pilot and industrial scale RPB gas-liquid flow in the future. In addition, a new method has been proposed to simulate different nozzle designs of the liquid distributor by user-defined functions (UDFs). Comprehensive analyses of hydrodynamic features such as liquid holdup, pressure drop and mean residence time were conducted under different working conditions (flow rates and rotational speeds), working systems (liquid viscosities) and inlet liquid distributions (nozzle designs). It is possible to lay the foundation for structural optimization design of RPB and coupling chemical reaction model and mass transfer model to simulate process intensification of various reactions and separations.

2. CFD Simulations

2.1 Physical model and boundary conditions

The CFD model presented in this paper has been validated using the experimental data from Yang et al. [20]. The experimental wire screen packing had dimensions of 42 mm inner diameter, 82 mm outer diameter, and 20 mm height. Due to the axial symmetry of the packing, only half of the height (10 mm) has been investigated in this paper. As shown in Fig. 1, the external boundary was defined as the gas velocity inlet, while the internal boundary was identified as the gas pressure outlet. The liquid generation zone and the liquid elimination zone have been established, with the former responsible for generating liquid and adding mass and momentum source while the latter removes liquid that reaches the outer boundary. The walls of both gas phase and liquid phase have been set as no-slip boundary walls. The specific area of the wire screen packing is 497 m^2/m^3, and its void fraction is 0.95. Two types of the liquid inlet method have been set: uniform and non-uniform liquid inlet, where details of the relevant settings for non-uniform liquid inlet are described in section 3.5 Nozzle designs of liquid distributor. The CFD simulation conditions of the RPB range from 500 to 2500 rpm for rotational speed, 1095 to 2580 mL/min for liquid flow rate, and 0 to 2 m/s for inlet gas flow rate (corresponding to 0 to 188.50 mL/min for inlet gas flow rate). Table 1 displays the working

fluids used in the simulation and their corresponding important physical parameters.

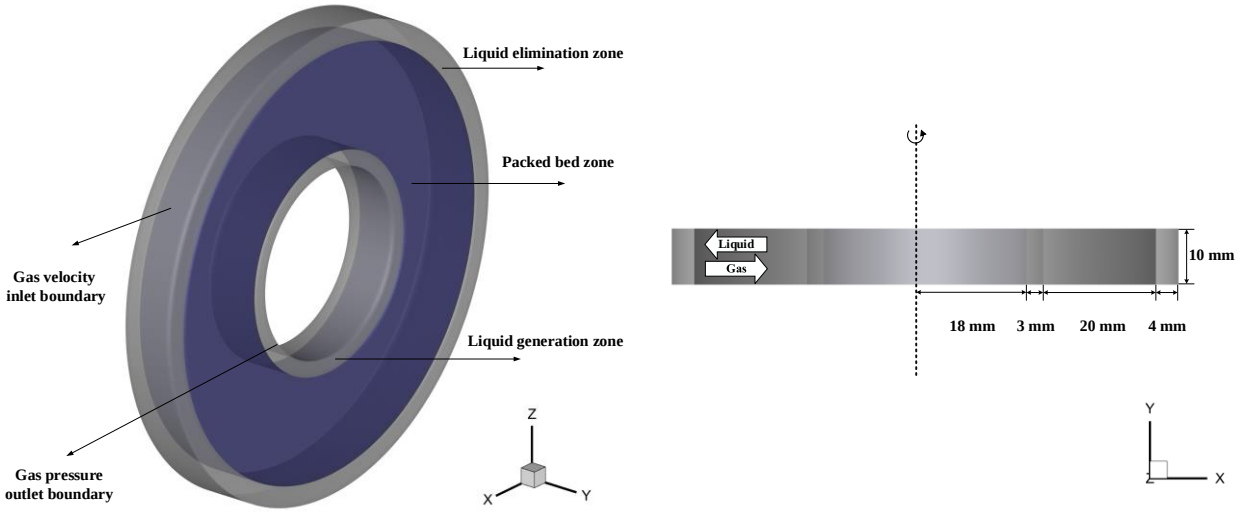

(a) Computational domain and boundary conditions (b) Size of the cross section

Fig.1. Schematic diagram for the design of the RPB.

Table 1 Physical parameters of working fluids.

Working fluids	Density(kg/m^3)	Viscosity(mPa•s)
Air	1.225	0.017894
Water	998.2	1.003
Glycerol(60%)	1140	9.38
Glycerol(70%)	1172.95	18.5
Glycerol(80%)	1213.6	55.8
Glycerol(90%)	1223.7	155.6

2.2 Governing equations and source term equations

The mass conservation equations are given as follows:

For the gas phase,

$$\frac{\partial}{\partial t}(\alpha_G \rho_G) + \nabla \cdot (\alpha_G \rho_G \vec{v}_G) = 0 \tag{1}$$

For the liquid phase,

$$\frac{\partial}{\partial t}(\alpha_L \rho_L) + \nabla \cdot (\alpha_L \rho_L \vec{v}_L) = S_{m,L} \tag{2}$$

The momentum conservation equations are given as follows:

For the gas phase,

$$\frac{\partial}{\partial t}\left(\alpha_G \rho_G \vec{v}_G\right)+\nabla\cdot\left(\alpha_G \rho_G \vec{v}_G \vec{v}_G\right)=-\alpha_G\cdot\nabla P+\nabla\cdot\bar{\bar{\tau}}_G-\vec{S}_{GL}-\vec{F}_{drag,G} \tag{3}$$

For the liquid phase,

$$\frac{\partial}{\partial t}\left(\alpha_L \rho_L \vec{v}_L\right)+\nabla\cdot\left(\alpha_L \rho_L \vec{v}_L \vec{v}_L\right)=-\alpha_L\cdot\nabla P+\nabla\cdot\bar{\bar{\tau}}_L+\vec{S}_{GL}-\vec{F}_{drag,L}+S_{k,L} \tag{4}$$

where α_G and α_L are the phase fraction of the gas and liquid phase, respectively; ρ_G and ρ_L are the densities of the gas and liquid, respectively; t is the time; $S_{m,L}$ is the liquid mass source; $\vec{v}_G$ and $\vec{v}_L$ are the velocities of the gas and liquid, respectively; P is the pressure; $\bar{\bar{\tau}}_G$ and $\bar{\bar{\tau}}_L$ are the stress-strain tensors of the gas and liquid phase, respectively; $\vec{S}_{GL}$ is the interfacial force between the gas and the liquid; $\vec{F}_{drag,G}$ and $\vec{F}_{drag,L}$ are the drag forces between the gas and the solid,the liquid and the solid, respectively; $S_{k,L}$ is the liquid momentum source.

The mass and momentum source term of liquid inlet and outlet are introduced into the generation zone and elimination zone by writing UDFs, respectively.

The source term equations of liquid generation zone are given as follows:

For mass source,

$$S_{m,L}=\frac{Q_L \rho_L}{\pi\left(r_1^{\,2}-r_0^{\,2}\right)h} \tag{5}$$

For momentum source,

$$S_{k,L,j}=\frac{Q_L \rho_L \vec{v}_L}{\pi\left(r_1^{\,2}-r_0^{\,2}\right)h}\frac{j}{\sqrt{x^2+z^2}} \tag{6}$$

The source term equations of liquid elimination zone are given as follows:

For mass source,

$$S_{m,L}=-\frac{\rho_L \alpha_L}{\Delta t} \tag{7}$$

For momentum source,

$$S_{k,L,j}=-\frac{\rho_L \alpha_L \vec{v}_{j,L}}{\Delta t} \tag{8}$$

where Q_L is the volume flow rate of the liquid; $S_{k,L,j}$ is the liquid momentum source (j = the coordinate or coordinate direction of radial (x), axial (y) and circumferential (z)); r_0 and r_1 are the inner and outer radius of the generation zone, respectively; h is the axial height of the liquid when it enters the packing; Δt is the time interval.

2.3 Porous media resistance models

In this paper, the modelling approach presented in the Lu model [34] was adopted to establish three distinct porous media resistance models based on diverse single-phase pressure drop models, which are referred to as K model, m-K model, and B model, respectively. The K model, m-K model and B model represent the porous media resistance models established based on the Kołodziej model [41], modified Kołodziej model [42], and Bussière model [43]. The basic equations of the three porous media resistance models are given as follows:

The K model:

$$\vec{S}_{GL} = f_e \varepsilon_G \left(\overrightarrow{v_G} - \overrightarrow{v_L}\right)\left[4\left(f_l + f_t\right)\frac{\rho_G \left|\overrightarrow{v_G} - \overrightarrow{v_L}\right|}{2d_w'}\frac{\left(1-\varepsilon_G\right)}{{\varepsilon_G}^3}\frac{\tau^3}{\cos^3\left(\theta\right)}\right] \tag{9}$$

$$\vec{F}_{drag,L} = f_e \varepsilon_L \overrightarrow{v_L}\left[4\left(f_l + f_t\right)\frac{\rho_L \left|\overrightarrow{v_L}\right|}{2d_w}\frac{\varepsilon_S}{{\varepsilon_L}^3}\frac{\tau^3}{\cos^3\left(\theta\right)}\right] \tag{10}$$

$$\vec{F}_{drag,G} = \left(1-f_e\right)\varepsilon_G \overrightarrow{v_G}\left[4\left(f_l + f_t\right)\frac{\rho_G \left|\overrightarrow{v_G}\right|}{2d_w}\frac{\left(1-\varepsilon_G\right)}{{\varepsilon_G}^3}\frac{\tau^3}{\cos^3\left(\theta\right)}\right] \tag{11}$$

The m-K model:

$$\vec{S}_{GL} = f_e \varepsilon_G \left(\overrightarrow{v_G} - \overrightarrow{v_L}\right)\left[4\left(f_l + f_t\right)\frac{\rho_G \left|\overrightarrow{v_G} - \overrightarrow{v_L}\right|}{2d_w'}\frac{\left(1-\varepsilon_G\right)}{{\varepsilon_G}^3}\frac{\tau^2}{\cos\left(\theta\right)}\right] \tag{12}$$

$$\vec{F}_{drag,L} = f_e \varepsilon_L \overrightarrow{v_L}\left[4\left(f_l + f_t\right)\frac{\rho_L \left|\overrightarrow{v_L}\right|}{2d_w}\frac{\varepsilon_S}{{\varepsilon_L}^3}\frac{\tau^2}{\cos\left(\theta\right)}\right] \tag{13}$$

$$\vec{F}_{drag,G} = \left(1-f_e\right)\varepsilon_G \overrightarrow{v_G}\left[4\left(f_l + f_t\right)\frac{\rho_G \left|\overrightarrow{v_G}\right|}{2d_w}\frac{\left(1-\varepsilon_G\right)}{{\varepsilon_G}^3}\frac{\tau^2}{\cos\left(\theta\right)}\right] \tag{14}$$

The B model:

$$\vec{S}_{GL} = f_e \varepsilon_G \left(\overrightarrow{v_G} - \overrightarrow{v_L}\right)\left[4\left(\frac{7.357}{\mathrm{Re}_k^{0.596}} + 0.04351\right)\frac{\rho_G \left|\overrightarrow{v_G} - \overrightarrow{v_L}\right|}{2d_w'}\frac{\left(1-\varepsilon_G\right)}{{\varepsilon_G}^3}\frac{\tau^2}{\cos\left(\theta\right)}\right] \tag{15}$$

$$\vec{F}_{drag,L} = f_e \varepsilon_L \overrightarrow{v_L}\left[4\left(\frac{7.357}{\mathrm{Re}_k^{0.596}} + 0.04351\right)\frac{\rho_L \left|\overrightarrow{v_L}\right|}{2d_w}\frac{\varepsilon_S}{{\varepsilon_L}^3}\frac{\tau^2}{\cos\left(\theta\right)}\right] \tag{16}$$

$$\vec{F}_{drag,G} = (1-f_e)\varepsilon_G \overrightarrow{v_G}\left[4\left(\frac{7.357}{\mathrm{Re}_k^{0.596}}+0.04351\right)\frac{\rho_G\left|\overrightarrow{v_G}\right|}{2d_w}\frac{(1-\varepsilon_G)}{{\varepsilon_G}^3}\frac{\tau^2}{\cos(\theta)}\right] \tag{17}$$

where,

$$f_l = \frac{1}{\mathrm{Re}_k}\left(\frac{3.44}{\sqrt{\chi^+}}+\frac{\frac{1.25}{4\chi^+}+16-\frac{3.44}{\sqrt{\chi^+}}}{1+\frac{0.00021}{\chi^+}}\right) \tag{18}$$

$$f_t = \frac{0.079}{\mathrm{Re}_k^{0.25}} \tag{19}$$

$$\chi^+ = \frac{d_w}{D_h\,\mathrm{Re}_k} \tag{20}$$

$$\mathrm{Re}_k = \frac{\rho v_e D_h}{\mu} \tag{21}$$

For the gas-liquid interfacial force,

$$\tau = 1+\frac{\varepsilon_S+\varepsilon_L}{2}, d_w' = \frac{4\varepsilon_S}{a_S'}, D_h = \frac{4\varepsilon_G}{a_S'}, a_S' = \left(\frac{\varepsilon_S+\varepsilon_L}{\varepsilon_S}\right)^{\frac{1}{2}} a_S \tag{22}$$

For the liquid-solid drag force,

$$\tau = 1+\frac{\varepsilon_S}{2}, d_w = \frac{4\varepsilon_S}{a_S}, D_h = \frac{4\varepsilon_L}{a_S} \tag{23}$$

For the gas-solid drag force,

$$\tau = 1+\frac{\varepsilon_S}{2}, d_w = \frac{4\varepsilon_S}{a_S}, D_h = \frac{4\varepsilon_G}{a_S} \tag{24}$$

The effective flow velocity of the gas-liquid interfacial force, liquid-solid drag force and gas-solid drag force are respectively defined as follows:

For the K model,

$$v_e = \frac{\left|\vec{v}_G-\vec{v}_L\right|\tau}{\varepsilon_G\cos(\theta)}, v_e = \frac{\left|\vec{v}_L\right|}{\varepsilon_L}\frac{\tau}{\cos(\theta)}, v_e = \frac{\left|\vec{v}_G\right|}{\varepsilon_G}\frac{\tau}{\cos(\theta)} \tag{25}$$

For the m-K model and B model,

$$v_e = \frac{\left|\vec{v}_G-\vec{v}_L\right|\tau}{\varepsilon_G}, v_e = \frac{\left|\vec{v}_L\right|\tau}{\varepsilon_L}, v_e = \frac{\left|\vec{v}_G\right|\tau}{\varepsilon_G} \tag{26}$$

where f_e is the wetted fraction of the packing; ε_G, ε_L and ε_S are the volume fraction of the gas, liquid and the solid phase, respectively; f_l is the Fanning friction factor for laminar flows; f_t is the Fanning friction factor for turbulent flows; τ is the hydraulic tortuosity factor; θ is the flow angle; d_w is the diameter of the wire screen; d'_w is the diameter of the wire screen with liquid film; Re_k is the effective Reynolds number; χ^+ is the dimensionless channel length; a_S and a'_S are the specific area of the dry wire and the wet wire, respectively; D_h is the hydraulic diameter; v_e is the effective flow velocity; μ is the fluid viscosity.

In the porous media model, the fluid-solid drag forces are decomposed into two components: the viscous resistance coefficient and the inertial resistance coefficient, both of which are loaded into the packed bed zone in the Fluent. By writing a UDF program for the gas-liquid interphase momentum exchange coefficient, the gas-liquid interfacial force is also loaded into the computational domain. Besides, for the calculation of fluid-solid drag forces, θ is taken as 80°.For the gas-liquid interfacial force, the assumption is made that the gas and liquid are flowing in opposite directions on the same axis, with a θ value of 0°.

2.4 Gas-liquid interfacial area

The relationship between the wetted fraction and the gas-liquid effective interfacial area is as follows:

$$f_e = \frac{A_{GL}}{a_S} \tag{27}$$

where, A_{GL} is the gas-liquid effective interfacial area.

The interfacial area can be obtained by the correlation equation established by the related research. Xie et al. [45] modeled a medium-dimensional 3D RPB using the VOF approach to simulate effective area of liquid flow through the screen packing under various operating conditions, and established a correlation equation as follows:

$$A_{GL} = 202.3485\left(\frac{g_c}{g_1}\right)^{0.0435}\left(\frac{U}{U_1}\right)^{0.4275}\left(\frac{\nu}{\nu_1}\right)^{0.1200}\left(\frac{\varphi}{\varphi_1}\right)^{-0.5856} \tag{28}$$

where, $g_1 = 205.6$ m/s^2, $U_1 = 0.0106$ m/s, $\nu_1 = 3.35\times10^{-6}$ m^2/s, $\varphi_1 = 75°$; g_c is the centrifugal acceleration; U is the average superficial liquid velocity; ν is the kinematic viscosity of the liquid; φ is the dynamic contact angle between the liquid and the screen, which is taken as 26° in this paper referring to the Zhang model [33].

2.5 Solution strategy

3D transient simulations of the RPB were performed in a double precision mode using ANSYS Fluent. The Realizable k-ε model provides an improved prediction of jet spread rate and it has the excellent ability to capture complex structural flows that involve rotational flows, boundary layer characteristics under high pressure gradients, flows and circulation [46]. Therefore, the Realizable k-ε model is utilized to simulate the flow characteristics of RPBs in this research work. The sliding mesh model is used to simulate the rotation of the packing. The pressure-based solution and absolute velocity formulation have been adopted.

The residual of the continuity equation is set to be less than 0.0005 and the residuals of the remaining equations are set to be less than 0.0001 during the simulation. The simulation uses a time step of 0.0003s and sets the maximum number of iterations to 20 for each time step. During the calculation, the change in liquid volume fraction of the packing is constantly monitored, and a pseudo-steady state is reached when this value no longer changes with increasing iteration number.

2.6 Mesh independence validation

The 3D computational mesh of the RPB was generated with ANYSY ICEM. The hexahedral mesh was used for the model. Three different numbers of meshes, 29440, 54000 and 84480, were employed to simulate the liquid holdup distribution of the RPB. The effect of the mesh number on liquid holdup in the packing was investigated using the m-K model at an inlet liquid flow rate of 2580 mL/min and a rotational speed of 1500 rpm, and the results are displayed in Fig. 2.

The comparison for the overall liquid holdup of three types of meshes simulation is shown in Fig. 2(a). At different numbers of meshes, the minimum ratio of the overall liquid holdup for water, 80% glycerol aqueous solution, and 90% glycerol aqueous solution with viscosities of 1.003, 55.8, and 155.6, respectively, was 0.9861, 0.9009, and 0.9269. It can be inferred that the number of meshes utilized has a negligible effect on the prediction of the overall liquid holdup. As shown in Fig. 2(b), the simulation results for the radial liquid holdup distribution were nearly identical for the meshes with the number of 54000 and 84480 respectively. At the same time, the simulated result of 29440 meshes has slight deviation compared with the results of the other two types of meshes, which indicates that the prediction of the radial liquid holdup distribution by the coarser grid lacks some stability. To ensure computational stability and minimize computational time the meshes with the number of 54000 is chosen for the gas-liquid flow simulation of RPBs.

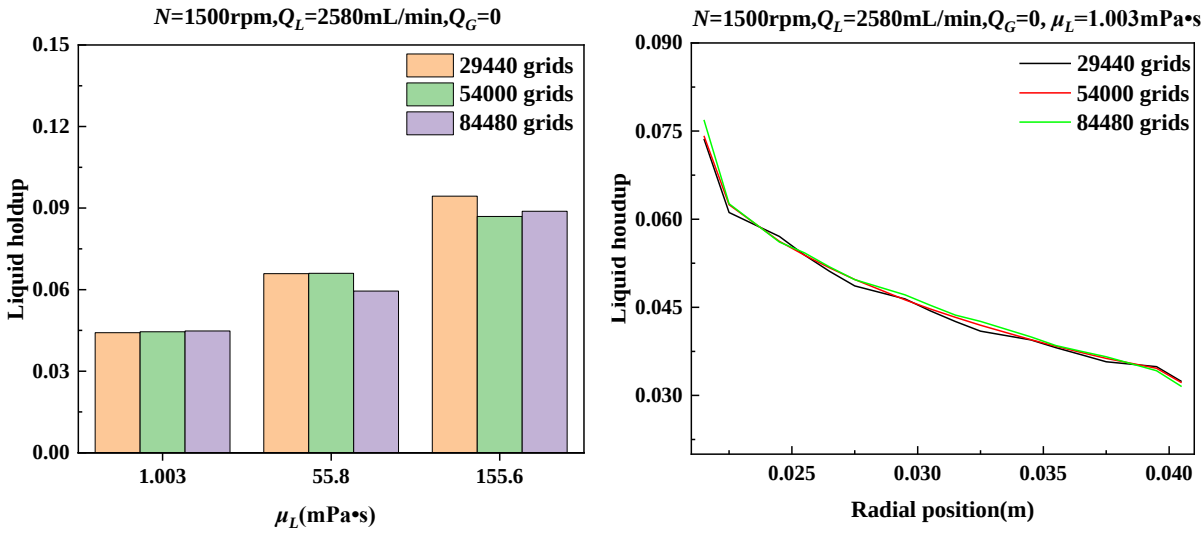

(a) Comparison of the overall liquid holdup (b) Comparison of the radial liquid holdup

Fig.2 Mesh independence validation.

3. Results and Discussion

In this paper, total 78 cases of simulations have been performed. Three different porous media resistance models were evaluated by comparing their simulation results with the experimental data published by Yang et al. [20]. After that, the m-K model has been chosen to investigate the effects of different viscosity work systems, flow rate, rotational speed and structure design on the gas-liquid hydrodynamic characteristics.

3.1 Model validation and accuracy comparison

In CFD simulation researches, liquid holdup is often used as a validation parameter because it is easier to obtain through experimental means. The liquid holdup in RPBs refers to the proportion of liquid volume inside the packing relative to the total volume of packing during operation. To ensure consistency with experimental conditions of Yang et al. [20], CFD simulations in this section were conducted using a water-air system without gas entering the packing, varying the liquid flow rate from 1095 to 2580 mL/min and the rotational speed from 500 to 2500 rpm. The simulation results are shown in Fig. 3~5. The liquid holdup distribution contours at various liquid flow rates and rotational speeds in the center plane of the packing (y=5mm) based on three different porous media resistance models are displayed in Fig. 3 and Fig. 4, respectively. In Fig. 5, the accuracy of the CFD simulation in predicting the liquid holdup is evaluated by comparing it to the experimental data. Based on the results shown in Fig. 3 and Fig. 4, it is apparent that the liquid holdup distribution obtained from the three models is similar for various operating conditions of liquid flow and rotational speed. Along both the radial and circumferential directions, the liquid holdup experiences a continuous decrease, with a particularly significant decrease observed in the entrance region and near wall region.

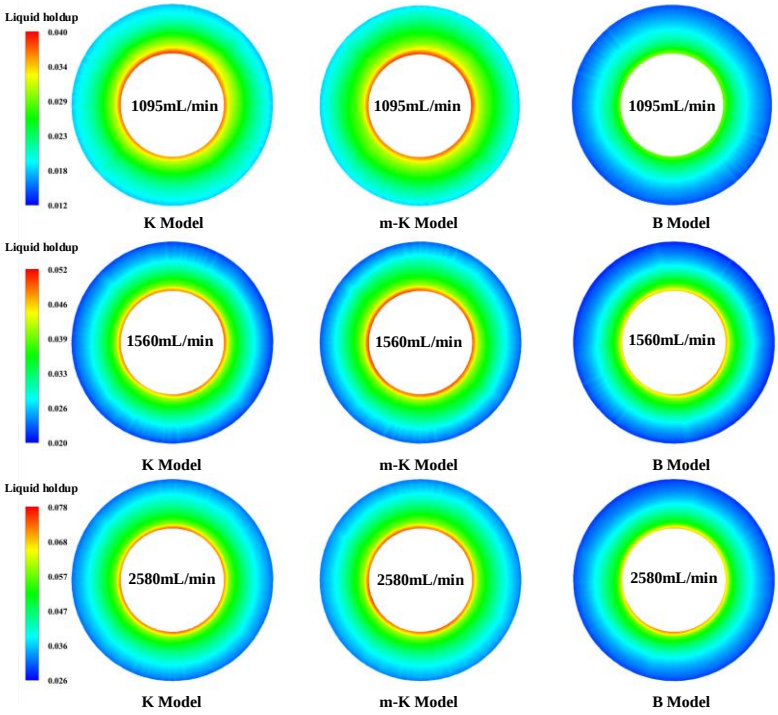

Fig. 3 Liquid holdup distribution for three models at N=1500rpm, μ_L=1.003mPa•s, Q_G=0 under different liquid flow rates (y=5mm).

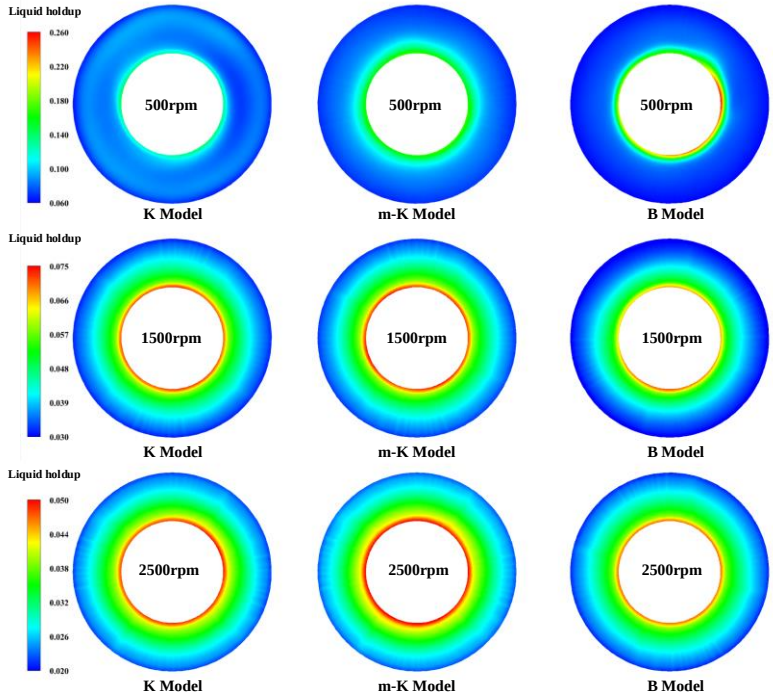

Fig. 4 Liquid holdup distribution for three models at Q_L=2580mL/min, μ_L=1.003mPa•s, Q_G=0 under different rotational speeds (y=5mm).

Fig. 5(a) and Fig. 5(b) show the comparison between the experimental data and simulation results of the overall liquid holdup in packing under different liquid flow rates and different rotational speeds, respectively. It can be seen that the overall liquid holdup in the packing zone increases with the increase of the liquid flow rate and decreases with the increase of the rotational speed, and the four curves are very close to each other. At small liquid flow rate (1095 mL/min) and low test rotational speed (500 rpm), CFD simulation data based on the K model, m-K model, and B model shows the largest deviation from experimental data with 26.43%, 23.81%, 36.72%, and 28.77%, 27.03%, and 34.44%, respectively. However, the deviations at other operating conditions are much smaller, and the maximum deviations between CFD simulation data and experimental data based on the K model, m-K model and B model for different liquid flow rates and different rotational speeds are 16.56%,12.78%,19.39% and 23.27%, 23.72%,17.89%, respectively. The deviations are reduced to within 25%. The reasons for this are that in the experiment, the porosity of the packing near wall region is lower than that of the packing bulk region causing the liquid flows out of the packing to be obstructed, while the liquid may be bounced back to the near wall region due to the influence of the rotor wall. Both of these reasons may lead to an increase of liquid holdup observed in the experiments which is the main cause of the deviation between CFD simulations and experimental data. In addition, when the RPB is under operating conditions of low rotational speed and small flow rate, the flow rate of liquid out of the near-wall area is lower and will be more influenced by these two factors, which will lead to the increase of deviation.

Fig. 5(c) is the comparison plot of the experimental data and simulation results for the distribution of liquid holdup along the

radial direction at Q_L=2580mL/min and N=1500rpm. It can be seen that the liquid holdup of the three CFD models decreases along the radial direction, while the experimental results do not vary in a smooth manner. The reason for this discrepancy is that for the CFD simulations in this section, liquid inlet does not be considered a water jet and it is considered as a liquid flowing uniformly into the RPB; in addition, liquid is set to disappear naturally when it flows out of the packing into the liquid elimination zone. In contrast, the liquid inlet in the experiment is a jet, resulting in the liquid near the entrance region not being completely dispersed, so that the liquid holdup decreases. Also, with the influence of the rotor wall of liquid outlet in the experiment, the liquid holdup near the near wall region increases. It can also be seen from Fig. 5(c) that the distribution trend of the CFD simulation of the liquid holdup along the radial direction is basically same with the experimental data in the bulk region. CFD simulations based on the K model, m-K model and B model obtain average deviations for the radial liquid holdup of 7.30%, 5.33% and 12.44%, respectively, all within 15%. The above analysis shows that all three porous media resistance models in 3D dimension are effective in predicting the liquid holdup of the RPB packing, and it is reasonable to use all three models to describe the effects of rotational speed and liquid flow rate for the liquid flow of the RPB.

Comparing the simulation results of liquid holdup with the experimental data, it can be concluded that the range of simulation deviations for the K model, m-K model, and B model are 5.81% to 28.77%, 0.92% to 27.61%, and 11.12% to 36.72%, respectively. In addition, it is also found that the order of simulation accuracy of the 3 models is significantly affected by the rotational speed through Fig. 5(b). For the rotational speed range of 500 to 1500 rpm, the order of the prediction accuracy of the three models is: m-K model > K model > B model. And for the rotational speed range of 2000 ~ 2500 rpm, the order of simulation accuracy of the 3 models is exactly opposite. The reason may be that there is a difference of the prediction for the gas-liquid interfacial between the CFD model and the experiment: the simulation correlation is fitted under the condition of centrifugal acceleration of 32.9~296.1 m/s^2, while the condition of centrifugal acceleration in the experiment [20] is 84.98~2124.70 m/s^2.

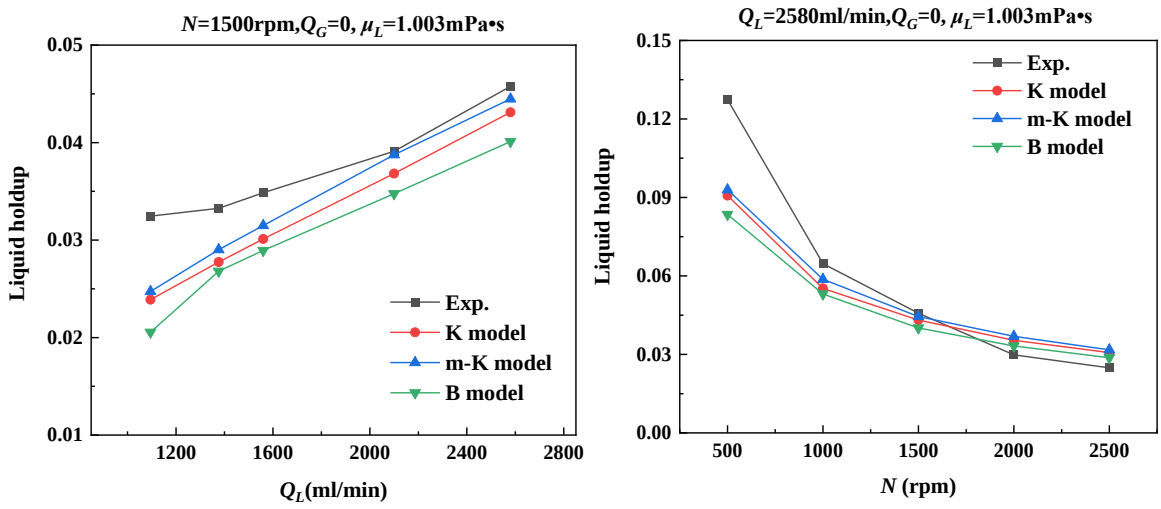

(a) Under different liquid flow rates

(b) Under different rotational speeds

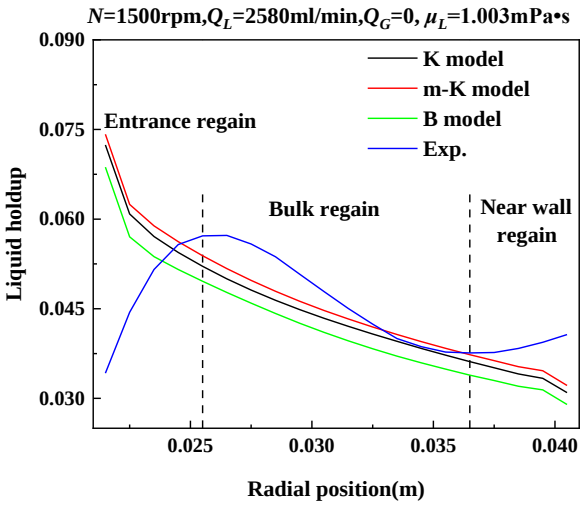

(c) Along the radial direction

Fig. 5 Comparison of the experimental data [20] and simulation results for liquid holdup of three models.

3.2 Liquid holdup of the packing

Due to most of rotational speed conditions for the subsequent CFD simulations are 1500 rpm, the m-K model is selected to perform the flow simulations for the subsequent sections. This section discusses the liquid distribution and the variation law of the liquid holdup for the RPB under the condition of different liquid viscosity work systems, liquid flow rates and rotational speeds. Fig. 6 shows the distribution of liquid holdup in the center plane (y=5 mm) and the vertical plane (z=0 mm) of the packing for different viscosity systems. Fig. 7 illustrates the variance of the radial liquid holdup for different viscosity systems. Fig. 8 (a) shows the effect of liquid viscosity on liquid holdup under different operating conditions. The impact of liquid flow rates and rotational speeds on the liquid holdup can be observed in Fig. 8(b) and Fig. 8(c), respectively.

The liquid distribution is reflected in three dimensions by analyzing the liquid holdup distribution in the center plane and vertical plane of the packing. As can be seen from Fig. 6, there are significant differences in the axial distribution of liquid holdup under different viscosities. At a lower viscosity (μ_L=1.003~18.5mPa•s), the liquid-holdup near the two sides (y=0mm, y=10mm) of the packing axial direction is lower than the inner region, while it is just the opposite at a higher viscosity (μ_L=55.8~155.6mPa•s). It reflects the effect of viscosity on the axial non-uniform distribution of the liquid. As viscosity increases, the flow resistance loss increases, leading to an increase of liquid film thickness, and liquid spreads throughout the axial direction of the packing. At the same time, the wall effect on both sides of the axial direction will lead to smaller liquid flow rate on both sides, thus making the liquid holdup at this place increase. Fig. 7 shows that the rate of the radial liquid holdup reduction in the inlet area is slower for high-viscosity liquid, as a result of its lower flow rate.

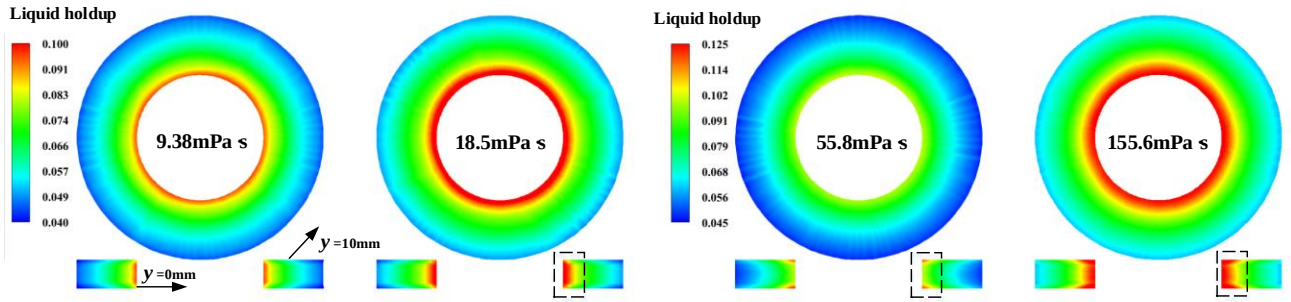

Fig. 6 Liquid holdup distribution in the packing under different liquid viscosity systems (N=1500rpm, Q_L=2580mL/min, Q_G=0).

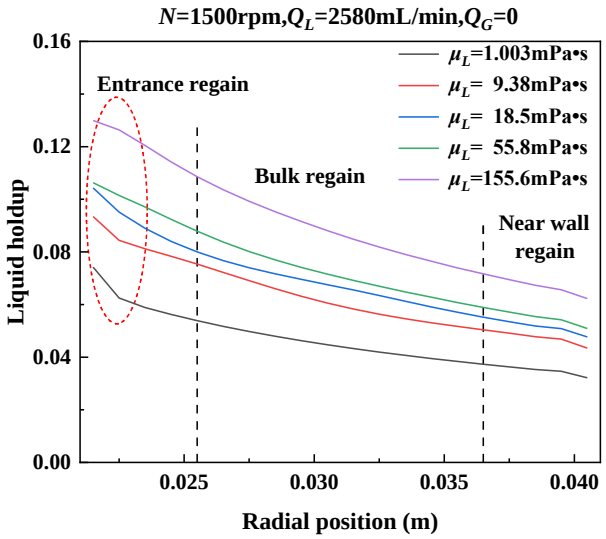

Fig. 7 Liquid holdup distribution along the radial direction for different liquid viscosity systems.

From Fig. 8 (a), it can be seen that when other conditions remain the same, as liquid viscosity rises, liquid flow rate decreases, liquid film thickness increases, and liquid holdup increases accordingly. As the increase of liquid viscosity from 1.003mPa•s to 155.6mPa•s, the range of liquid holdup increases from 0.0290~0.0929 to 0.0517~0.2027. The effect of liquid viscosity on the liquid holdup is more significant at low rotational speeds than high rotational speeds. It is because the liquid flow rate becomes faster at high rotational speed, which decreases the impact tendency of viscosity to the liquid holdup. Curves are very close for the two working conditions of N=1500rpm, Q_L=1376mL/min and N=2500rpm, Q_L=2580mL/min in Fig. 8(a). This is because of the increasing of liquid flow rate and rotational speed on effect of viscosity on liquid holdup respectively produced two different influential trends of promotion and inhibition. From Fig. 8(b) and Fig. 8(c), it can be seen that the liquid holdup of packing increases gradually with the increase of liquid flow rate and decreases gradually with the increase of rotational speed. In addition, as the rotational speed is increased from 500 rpm to 1000 rpm, the liquid holdup undergoes a sharp drop, which can largely be attributed to the transformation of the liquid flow pattern within pore spaces from film to droplet.

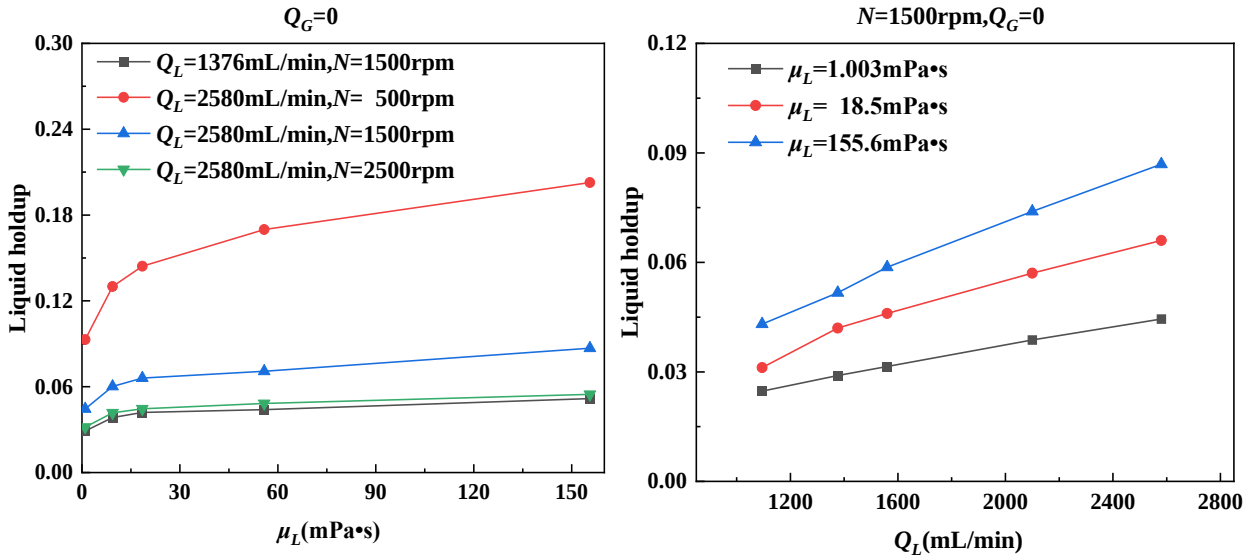

(a) Liquid viscosity

(b) Liquid flow rate

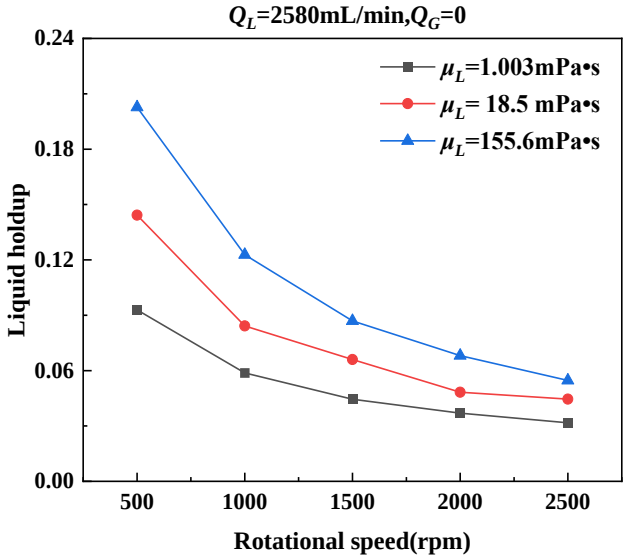

(c) Rotational speed

Fig. 8 Effect of different parameters on the overall liquid holdup.

3.3 Mean residence time of the liquid

Mean residence time of the liquid can be determined by the following expression [20]:

$$\bar{t} \approx \frac{r_2 - r_1}{U / \varepsilon_L} = \frac{r_2 - r_1}{\left(Q_L / 2\pi r_{avg} h\right) / \varepsilon_L} \tag{29}$$

where r_2 and r_1 are the inner and outer radius of the packing; r_{avg} is the average radius of the packing.

Fig. 9(a) and Fig. 9(b) show the effect of rotational speed and liquid flow rate on the mean residence time under different liquid viscosities, respectively. From Fig. 9(a), it can be seen that the increase of rotational speed leads to a greater centrifugal acceleration of the liquid, resulting in a decrease of the liquid film thickness and an increase of the liquid flow rate, which causes

a decrease of the mean residence time. Among them, the mean residence time decreases more with rotational speed in the low speed range, mainly because the decrease of mean residence time signifies to a certain extent the thinning of the film on the packing surface. On the one hand, with the gradually increasing rotational speed, the shear stress inside the film on the packing surface increases rapidly, which plays the hindering function to the further reduction of the liquid film thickness. On the other hand, in the low speed range, the flow pattern of a large portion of the liquid in the pores has already changed from film to droplet, making further increases in rotational speed have less effect on the liquid produced in this droplet pattern. As can be seen from Fig. 9(b), the mean residence time decreases with the increase of liquid flow. The liquid flow rate increases from 1376 mL/min to 2580 mL/min, so the inlet velocity of the liquid increases about twice, but the mean residence time of water, 70% glycerol solution and 90% glycerol solution only decreases by 18.24%, 16.21% and 10.30%, respectively. This is because after the liquid flows into the packing, the kinetic energy brought by the liquid flow is quickly absorbed by the packing, and then the energy of forward motion is provided by the centrifugal acceleration of the packing, so the initial velocity brought by the liquid inlet has a small effect on the mean flow rate of the liquid.

The Fig.9 also shows that the greater of the liquid viscosity, the longer of the mean residence time, with the increase of the liquid viscosity from 1.003mPa•s to 155.6mPa•s, the range of the mean residence time of the liquid increased significantly from 0.0576 ~ 0.1686 s to 0.0991 ~ 0.3678 s. In addition, it is observed that the mean residence time decreases the most for high viscosity liquids by comparing the level of decrease in mean residence time with increasing rotational speed for different viscosities. Therefore, in the high viscosity liquid working system, the liquid residence time can be appropriately adjusted by controlling the rotational speed of RPBs, which is a significant advantage for research using high viscosity liquids and RPBs for reaction process intensification, etc.

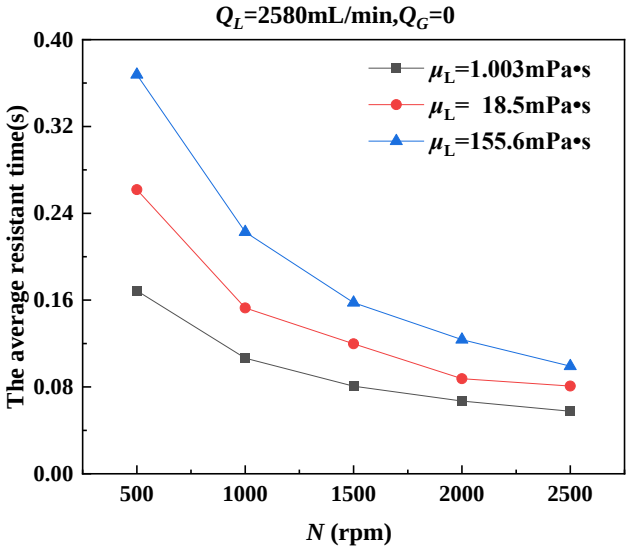

(a) Rotational speed

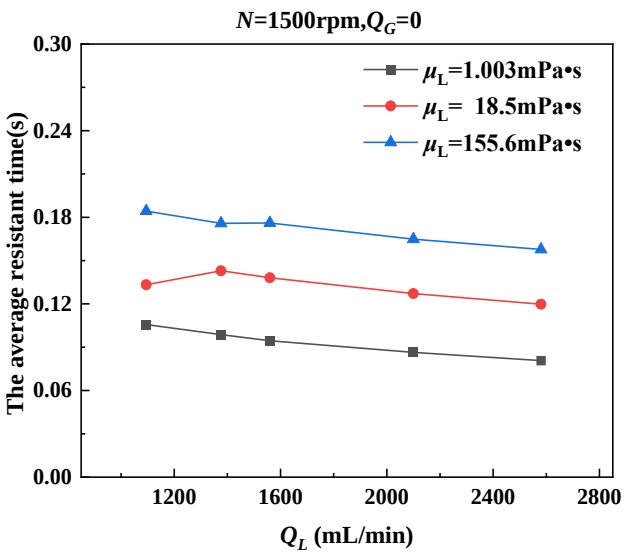

(b) Liquid flow rate

Fig. 9 Effect of different parameters on the mean residence time of liquid.

3.4 Pressure drop

As CFD simulations in this paper have not accurately modeled and simulated the inner and outer cavities, the pressure drop data obtained from the simulations is the rotor packing part. Lashkarbolooki [44] developed a general model to predict the rotor packing pressure drop in the RPB. Lashkarbolooki's correlation equation for pressure drop prediction [44] is as follows:

$$-\Delta P_{III} = \Delta P_I + \Delta P_{II} + \Delta P_{III} \tag{30}$$

$$\Delta P_I = A\left(\frac{GFR}{2\pi h}\right)\ln\left(\frac{r_2}{r_1}\right) + B\left(\frac{GFR}{2\pi h}\right)^2\left(\frac{1}{r_2} - \frac{1}{r_1}\right) \tag{31}$$

$$\Delta P_{II} = \frac{1}{2}\rho_G\left(K\omega\right)^2\left(r_2 - r_1\right)^2 \tag{32}$$

$$\Delta P_{III} = \left(\beta_1 + \beta_2\right)\left(v_G - v_L\right) \tag{33}$$

where ΔP_I, ΔP_{II} and ΔP_{III} are drag pressure drop, centrifugal pressure drop and slip pressure drop, respectively; *GFR* is the gas volumetric flow rate; *A* and *B* are the empirical parameters of viscous energy loss term and inertial loss term, respectively; *K* is the empirical parameter of centrifugal term; ω is the rotational angular velocity; β_1 and β_2 are the gas-solid and gas-liquid slip parameters, respectively.Due to the small size and small gas flow rate range of the RPB used in this paper, *K* is taken as 1 in this validation work [34,44]. The rest of the empirical parameters are estimated according to the correlation equations given in the literature.

As shown in Fig. 10, the pressure drop data of CFD simulations for the water-air system at different operating conditions are quantitatively compared with the data calculated by the Lashkarbolooki pressure drop correlation [44]. The impact of liquid flow rate on pressure drop is illustrated in Fig. 10(a), revealing that the pressure drop value remains relatively constant as the liquid flow rate increases. The reason for this is that, at high rotational speeds, changes in liquid inlet flow rate have small impact on the liquid flow velocity through the packing. Fig. 10(b) and Fig. 10(c) show effects of rotational speed and gas flow rate on pressure drop, respectively. The results show that pressure drop increases with the increase of rotational speed and gas flow rate. When the rotational speed increases, the centrifugal force increases leading to an increase in the rotational pressure drop ΔP_{II}, which results in an increase of pressure drop. And when the gas flow rate increases, the pressure drop increases due to the increase of the resistance pressure drop term ΔP_I. In addition, the deviation of the correlation calculated value of the pressure drop with the simulated value ranges from 1.63% to 34.59%. This shows that the porous media resistance model established in this paper can reasonably and effectively simulate the pressure drop of the packing.

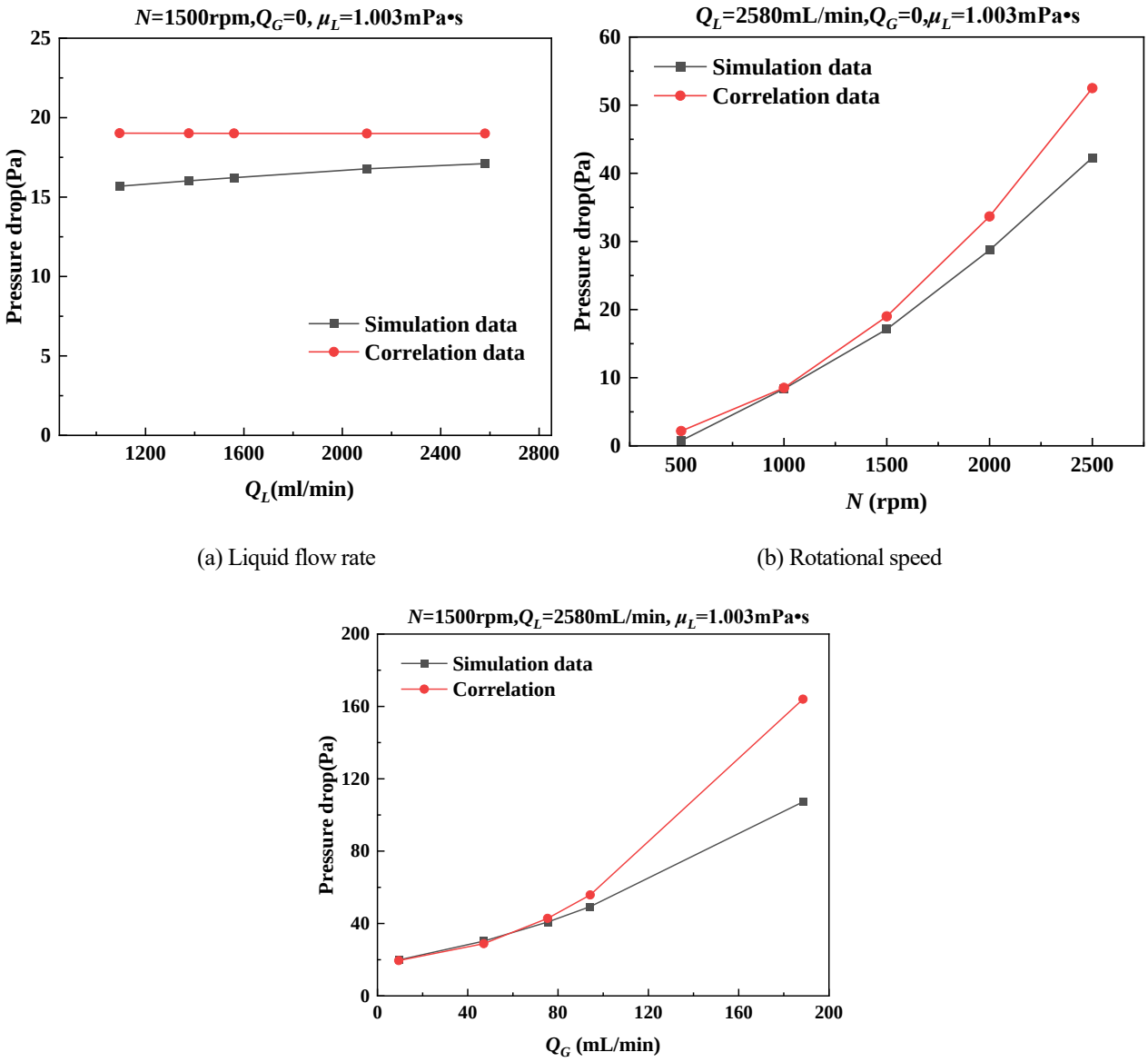

(a) Liquid flow rate

(b) Rotational speed

(c) Gas flow rate

Fig. 10 Comparison of the calculated data of Lashkarbolooki pressure drop correlation [44] and pressure drop simulation results.

3.5 Nozzle designs of liquid distributor

The liquid distributor locates near the inner surface of RPBs, and is one of the important component parts in RPBs. The nozzle structure of the liquid distributor has a direct impact on the initial liquid distribution, which subsequently affects the overall liquid distribution throughout the entire packing area. The nozzle of the liquid distributor is generally divided into two structural types: open-slit and open-hole. As shown in Fig. 11, we have designed three types of open-slit liquid distributors with different nozzle axial height (h), as well as four types of open-hole liquid distributors with different number of open holes (n_{open}) when h=10mm. Among them, the width of the nozzles is all designed to 1 mm. By utilizing UDFs in the CFD simulations, the location of the nozzles in the liquid generation zone could be precisely controlled, allowing for an effective simulation of both their number

and size.

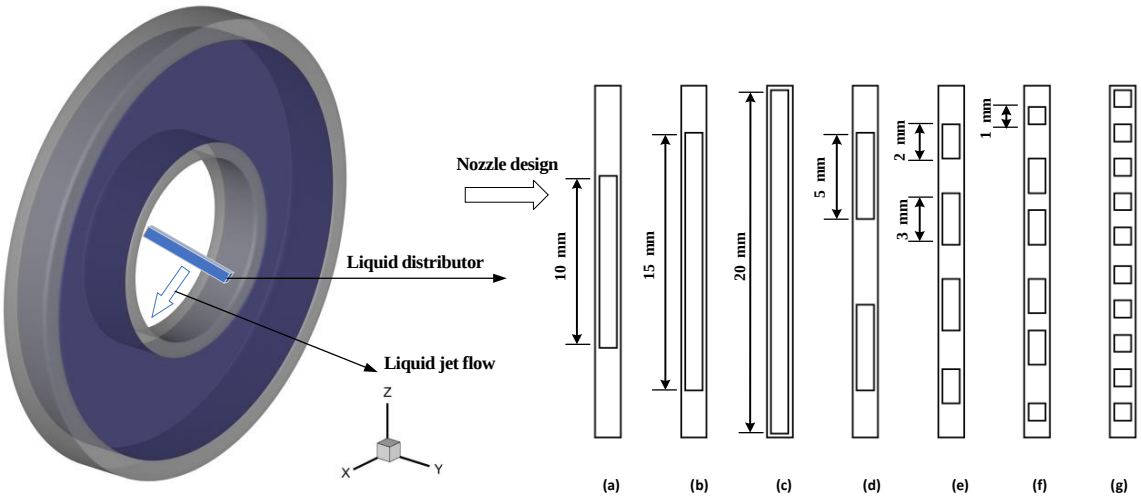

Fig. 11 Schematic diagram of nozzle designs of the liquid distributor: the type of open-slit (a) h=10mm(n_{open}=1), (b) h=15mm(n_{open}=1), (c) h=20mm(n_{open}=1); the type of open-hole: (d) h=10mm(n_{open}=2), (e) h=10mm(n_{open}=4), (f) h=10mm(n_{open}=6), (g) h=10mm(n_{open}=10).

The liquid holdup distribution contours of the packing under same conditions with different nozzle numbers (n) can be viewed in Fig. 12. The results indicate that an increase in nozzle number leads to a more uniform liquid distribution along directions of radial and circumferential. The distribution contours for axial liquid holdup at different nozzle heights and nozzle opening numbers are shown in Fig. 13. As the nozzle heights are raised, the axial liquid distribution becomes increasingly uniform. When the total height of the nozzle is the same, the more and smaller of the open holes in the nozzle, the axial liquid distribution is more uniform. The above simulation outcomes indicate that increasing the height, decreasing the size, and increasing the number of nozzles all lead to a more uniform liquid holdup distribution throughout the entire packing area.

Fig. 14 shows the effect of different nozzle designs on the liquid holdup. It can be observed that when the number of nozzles is fixed, raising the nozzle height leads to a decrease in axial liquid jet velocity, which in turn contributes to a more uniform liquid distribution throughout the packing and an increase in liquid holdup. With a nozzle height of 20 mm, the liquid holdup rises by 11.55% and 2.71% as the number of nozzles is increased from 1 to 2 and from 2 to 4, respectively. At a total nozzle height of 10 mm, the liquid holdup increases by 18.05% and 4.89% as the number of nozzle openings is increased from 2 to 6 and from 6 to 10, respectively. The above results indicate that as the number of nozzles and nozzle openings further increase, the rising trend of the liquid holdup diminishes. This section also included simulations evaluating the impact of different liquid viscosities for the distribution of liquid holdup under same operating conditions, as shown in Fig. 15. Clearly from the Fig. 15 that enhanced liquid viscosity reduces the flow velocity at the nozzle inlet, promoting greater uniformity of liquid distribution in both radial and circumferential directions.

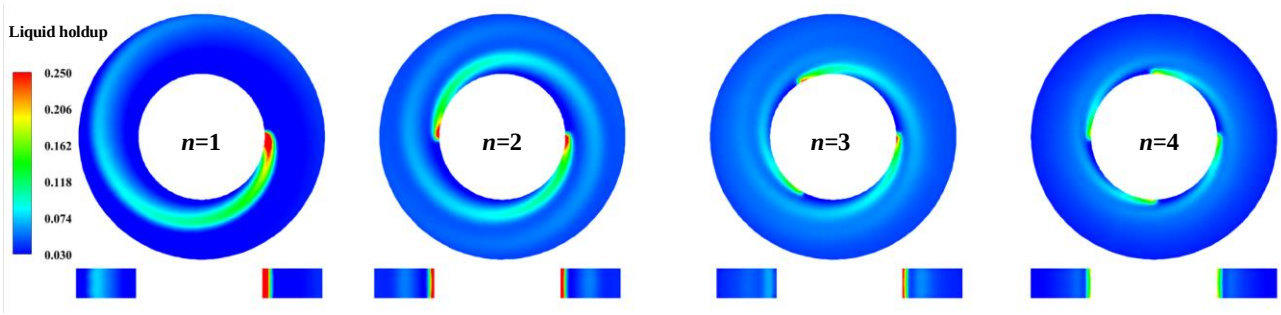

Fig. 12 Liquid holdup distribution of the packing under different numbers of nozzles (N=1500rpm, Q_L=2580mL/min, Q_G=0, μ_L=1.003mPa•s, n_{open}=1).

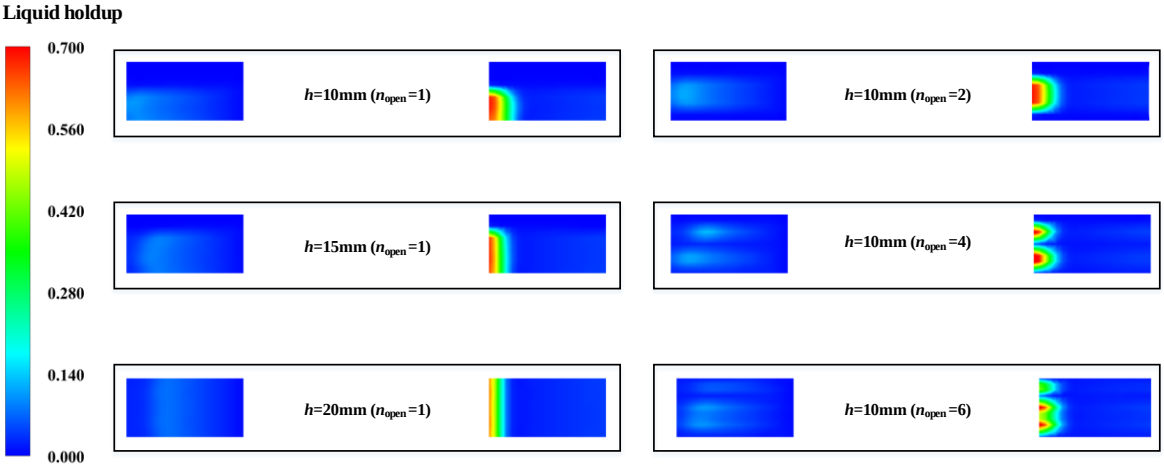

Fig. 13 Liquid holdup distribution of the packing under different nozzle heights and numbers of nozzle openings (N=1500rpm, Q_L=2580mL/min, Q_G=0, μ_L=1.003mPa•s, n=1).

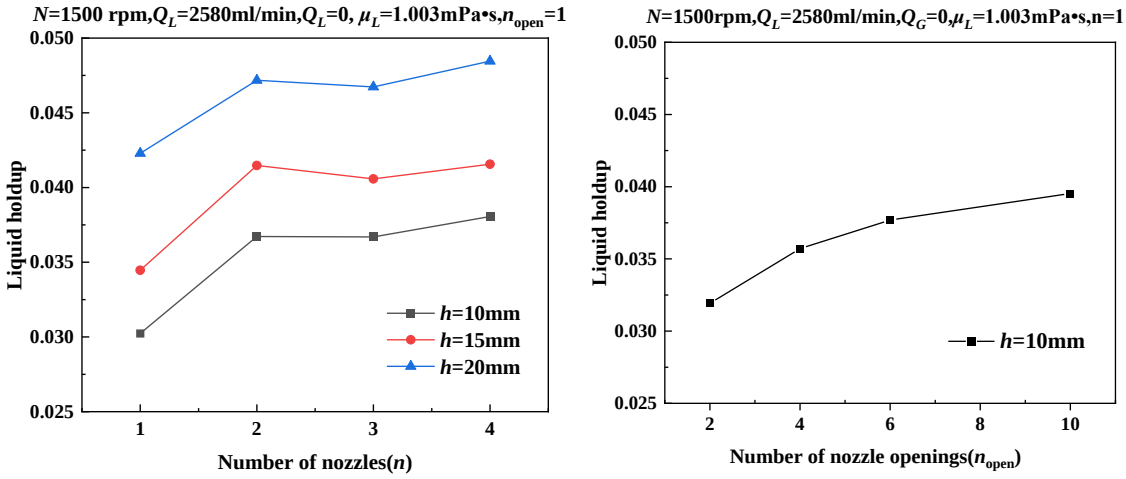

(a) Number and height of nozzles (b) Number of nozzle openings

Fig. 14 Effects of different nozzle designs on the overall liquid holdup.

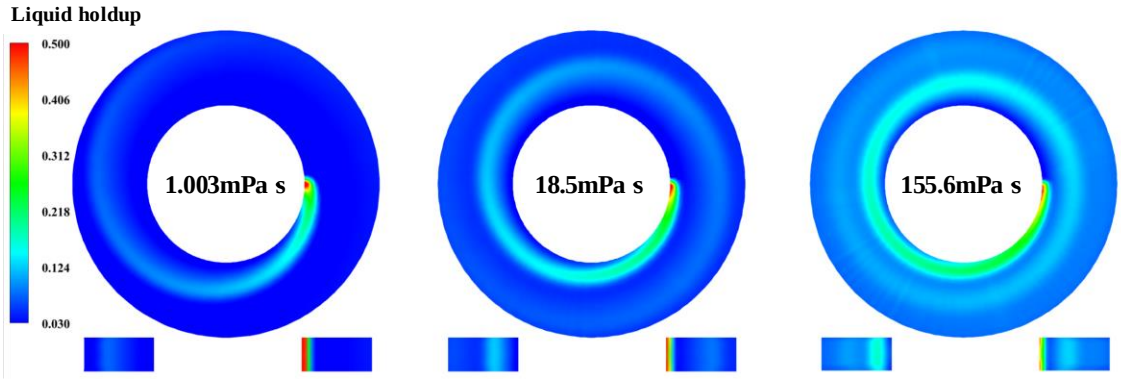

Fig.15 Liquid holdup distribution of the packing under different liquid viscosities (N=1500rpm, Q_L=2580mL/min, Q_G=0, h=20mm, n=1, n_{open}=1).

4.Data Availability and Reproducibility Statement

The numerical data from Figures 2, 5, 7~10, and 14 are tabulated in the Supplementary Material. The detailed calculation formulas for three single-phase pressure drop models and drag forces can be obtained from the Supplementary Material. The data that support the findings of this study are available from the corresponding author upon reasonable request.

5. Conclusions

In this work, based on the Eulerian two-fluid method and different single-phase wire screen packing pressure drop models, three porous media resistance models were developed to simulate the flows of gas and liquid in RPBs. Characteristics of gas-liquid flow such as liquid holdup, pressure drop and liquid mean residence time under different working conditions, working systems and inlet liquid distribution designs were predicted.

The CFD simulations in this paper contribute to the following conclusions:

(i) Three porous media resistance models established can reasonably and effectively simulate the gas-liquid two phase flow of the RPB packing in the 3D dimension. The simulation deviations of liquid holdup of the K model, m-K model, and B model range from 5.81% to 28.77%, 0.92% to 27.61%, and 11.12% to 36.72%, respectively. In the process of simulating the m-K model, deviations in pressure drop are found to range from 1.63% to 34.59%.

(ii) The accuracy order of liquid holdup simulation for the three models is significantly influenced by the rotational speed. The prediction accuracy of three porous media resistance models under the rotational speed range of 500 to 1500 rpm is: m-K model > K model > B model, while for the rotational speed range of 2000 to 2500 rpm, the order of simulation accuracy for liquid holdup among the three models is completely reversed.

(iii) The greater of the liquid viscosity, the more uniform of liquid distribution in the axial direction of the packing, and liquid holdup on both sides of the axial direction is higher than the internal area. In addition, nozzle height, nozzle size, and nozzle number all exert a significant impact on the distribution of liquid holdup within the packing, with greater uniformity achieved

through taller nozzles, smaller nozzle sizes, and increasing numbers of nozzles.

(iv) An increase in rotational speed leads to a decrease in liquid holdup within the packing, while an increase in liquid flow rate results in greater liquid holdup. In addition, increasing either rotational speed or liquid flow rate decreases the mean residence time of the liquid. Increasing either rotational speed or gas flow rate results in an increase in the pressure drop experienced through the packing. As the liquid viscosity increases, both liquid holdup and the mean residence time within the packing increase as well, with this effect being more pronounced at lower rotational speeds.

Acknowledgment

The present work is supported by the National Natural Science Foundation of China (52274068, U21B2085) and the Natural Science Foundation of Shandong Province of China (ZR2021ME128).

Nomenclature

a_S	specific area of the dry wire (m^2/m^3)
a'_S	specific area of the wet wire (m^2/m^3)
A	empirical parameter of viscous energy loss term
A_{GL}	effective interfacial area between gas and liquid (m^{-1})
B	empirical parameters of inertial loss term
D_h	hydraulic diameter (m)
d_w	diameter of the wire screen (m)
d'_w	diameter of the wire screen with liquid film (m)
f_e	wetted fraction of the packing
f_l	Fanning friction factor for laminar flows
f_t	Fanning friction factor for turbulent flows
$\vec{F}_{drag,G}$	drag forces between the gas and the solids of the packing material (N/m^3)
$\vec{F}_{drag,L}$	drag forces between the liquid and the solids of the packing material (N/m^3)
g_c	centrifugal acceleration (m/s^2)
g_1	characteristic centrifugal acceleration (=205.6 m/s^2)
GFR	volumetric flow rate of gas (m^3/s)
h	axial height of the liquid when it enters the packing or nozzle axial height (m)
K	empirical parameter of centrifugal term
n	number of nozzles

n_{open}	number of nozzle openings
N	rotational speed (rpm)
P	pressure (Pa)
ΔP	pressure drop (Pa)
ΔP_I	the drag pressure drop (Pa)
ΔP_{II}	centrifugal pressure drop (Pa)
ΔP_{III}	slip pressure drop (Pa)
Q	volume flow rate(m^3/s)
r_1	outer radius of the liquid generation zone or inner of the packing (m)
r_2	outer radius of the packing;
r_0	inner radius of the liquid generation zone (m)
r_{avg}	average radius of the packing (m)
Re_k	effective Reynolds number
$S_{k,L}$	liquid momentum source (N/m^3)
$S_{k,L,j}$	liquid momentum source of the j coordinate direction (N/m^3)
$S_{m,L}$	liquid mass source ($kg/(m^3 \bullet s)$)
$\vec{S}_{GL}$	interfacial force between the gas and the liquid (N/m^3)
t	time (s)
$\bar{t}$	mean residence time of the liquid (s)
Δt	time interval (s)
U	average superficial liquid velocity (m/s)
U_1	characteristic flow rate per unit area (=0.0106 m/s)
v_e	effective flow velocity (m/s)
$\vec{v}$	velocity of gas phase or liquid phase (m/s)
j	coordinate (m)
x	radial coordinate (m)
y	axial coordinate (m)
z	circumferential coordinate (m)

Greek symbols

α	phase fraction

β_1	gas-solid slip parameter
β_2	gas-liquid slip parameter
v	kinematic viscosity of the liquid (m^2/s)
v_1	characteristic kinematic viscosity of the liquid (3.35×10^{-6}=m^2/s)
θ	flow angle (°)
φ	dynamic contact angle (°)
φ_1	characteristic dynamic contact angle (=75°)
ε	volume fraction
ε_L	liquid holdup (volume fraction of liquid)
ρ	density (kg/m^3)
χ^+	dimensionless channel length
μ	fluid viscosity (kg/(m•s))
τ	hydraulic tortuosity factor of packing
$\bar{\bar{\tau}}$	stress-strain tensor
ω	rotational angular velocity(rad/s)

Subscripts

G	gas phase
L	liquid phase
i	= G, L
S	solids phase of packing material
j	= x, y, z

References

[1] Reay D. The role of process intensification in cutting greenhouse gas emissions. *Applied Thermal Engineering*. 2008;28(16):2011-2019. doi:10.1016/j.applthermaleng.2008.01.004

[2] Zhang W, Xie P, Li Y, Teng L, Zhu J. 3D CFD simulation of the liquid flow in a rotating packed bed with structured wire mesh packing. *Chemical Engineering Journal*. 2022;427:130874. doi:10.1016/j.cej.2021.130874

[3] Zhao H, Shao L, Chen JF. High-gravity process intensification technology and application. *Chemical Engineering Journal*. 2010;156(3):588-593. doi:10.1016/j.cej.2009.04.053

[4] Wang D, Liu T, Ma L, Wang F, Yun J, Shao L. Degradation Kinetics Study of Fast Ozonation Reaction in a Rotating Packed

Bed. *Ozone: Science & Engineering*. 2022;44(5):438-452. doi:10.1080/01919512.2021.1967724

[5] Li YJ, Qi TT, Dong YN, et al. Synthesized Ni/MMO catalysts via ultrathin Ni-Al-LDH in a rotating packed bed for hydrogenation of maleic anhydride. *Fuel*. 2022;326:125035. doi:10.1016/j.fuel.2022.125035

[6] Tian Y, Mei S, Zhang L, et al. Improved H_2SO_4-catalyzed alkylation reaction in a rotating packed bed reactor by adding additives. *Can J Chem Eng*. 2022;100(11):3395-3407. doi:10.1002/cjce.24342

[7] Jing J, Jiao W, Li Z, et al. High-gravity intensified iron-carbon micro-electrolysis for degradation of dinitrotoluene. *Front Chem Sci Eng*. 2022;16(11):1595-1605. doi:10.1007/s11705-022-2204-9

[8] Cheng S, Qi G, Wu L, Guo S. Deep purification of low concentration fine particles in a cross flow rotating packed bed. *Journal of the Taiwan Institute of Chemical Engineers*. 2023;143:104723. doi:10.1016/j.jtice.2023.104723

[9] Cheng S, Qi G, Wu L, Wang S. High gravity wet purification of fine particles and naphthalene in gas. *Chemical Engineering and Processing - Process Intensification*. 2023;184:109301. doi:10.1016/j.cep.2023.109301

[10] Dong YN, Chen WC, Zhang LL, et al. Green and efficient sulfur dioxide removal using hydrogen peroxide in rotating packed bed reactor: Modeling and experimental study. *Chemical Engineering Science*. 2021;235:116467. doi:10.1016/j.ces.2021.116467

[11] Chen TL, Xiong YX, Chen YH, Chiang PC, Chen YH. Performance evaluation and process simulation for synergetic removal of NOx, CO2 and PM using green alkaline solution in a high-gravity rotating packed bed. *Fuel*. 2020;280:118643. doi:10.1016/j.fuel.2020.118643

[12] Wen ZN, Xu HZ, Li YB, et al. Carbon dioxide capture in a HiGee reactor with packing featuring controllable cross-sectional area. *Separation and Purification Technology*. 2023;305:122510. doi:10.1016/j.seppur.2022.122510

[13] Wojtasik-Malinowska J, Piątkowski M, Blatkiewicz M, Jaskulski M, Wawrzyniak P, Górak A. Reactive absorption of carbon dioxide in aqueous n-methyldiethanoloamine solutions catalysed with carbonic anhydrase in a rotating packed bed (RPB). *Chemical Engineering and Processing - Process Intensification*. 2023;184:109266. doi:10.1016/j.cep.2023.109266

[14] Chen WC, Fan YW, Zhang LL, et al. Computational fluid dynamic simulation of gas-liquid flow in rotating packed bed: A review. *Chinese Journal of Chemical Engineering*. 2022;41:85-108. doi:10.1016/j.cjche.2021.09.024

[15] Li Y, Wang S, Sun B, et al. Visual study of liquid flow in a rotor-stator reactor. *Chemical Engineering Science*. 2015;134:521-530. doi:10.1016/j.ces.2015.05.046

[16] Xu Y, Li Y, Liu Y, et al. Liquid jet impaction on the single-layer stainless steel wire mesh in a rotating packed bed reactor. *AIChE J*. 2019;65(6). doi:10.1002/aic.16597

[17] Wang Y, Li YB, Su MJ, Chu GW, Sun BC, Luo Y. Liquid droplet dispersion in a rotating packed bed: Experimental and

numerical studies. *Chemical Engineering Science*. 2021;240:116675. doi:10.1016/j.ces.2021.116675

[18] Liu ZH, Xu HZ, Chen WC, Li YB, Zhang LL, Chu GW. Dispersion characteristics of liquid jet impacting on the rotating single-layer wire mesh with different surface wettabilities. *Chemical Engineering Science*. 2022;251:117495. doi:10.1016/j.ces.2022.117495

[19] Li YB, Wen ZN, Xu HZ, Chu GW, Zhang LL, Chen JF. Flow pattern transition and liquid element characteristics in a disk-distributor rotating packed bed: A visual study for viscous fluid. *Chemical Engineering Science*. 2022;260:117854. doi:10.1016/j.ces.2022.117854

[20] Yang Y, Xiang Y, Chu G, et al. A noninvasive X-ray technique for determination of liquid holdup in a rotating packed bed. *Chemical Engineering Science*. 2015;138:244-255. doi:10.1016/j.ces.2015.07.044

[21] Liu Y, Luo Y, Chu G, Liu W, Shao L, Chen J. Liquid holdup and wetting efficiency in a rotating trickle-bed reactor. *AIChE J*. 2019;65(8). doi:10.1002/aic.16618

[22] Yan Z yi, Lin C, Ruan Q. Hydrodynamics in a Rotating Packed Bed. I. A Novel Experimental Method. *Ind Eng Chem Res*. 2012;51(31):10472-10481. doi:10.1021/ie202257t

[23] Zhang W, Xie P, Li Y, Teng L, Zhu J. CFD analysis of the hydrodynamic characteristics in a rotating packed bed with multi-nozzles. *Chemical Engineering and Processing - Process Intensification*. 2020;158:108107. doi:10.1016/j.cep.2020.108107

[24] Rabiee R, Monzavi M, Shabanian J, et al. Two-Phase flow characterization of a rotating packed bed through CFD simulation in OpenFOAM. *Chemical Engineering Science*. 2022;253:117589. doi:10.1016/j.ces.2022.117589

[25] Shi X, Xiang Y, Wen LX, Chen JF. CFD analysis of liquid phase flow in a rotating packed bed reactor. *Chemical Engineering Journal*. 2013;228:1040-1049. doi:10.1016/j.cej.2013.05.081

[26] Liu Y, Luo Y, Chu GW, Larachi F, Zou HK, Chen JF. Liquid microflow inside the packing of a rotating packed bed reactor: Computational, observational and experimental studies. *Chemical Engineering Journal*. 2020;386:121134. doi:10.1016/j.cej.2019.03.010

[27] Ouyang Y, Zou HK, Gao XY, Chu GW, Xiang Y, Chen JF. Computational fluid dynamics modeling of viscous liquid flow characteristics and end effect in rotating packed bed. *Chemical Engineering and Processing - Process Intensification*. 2018;123:185-194. doi:10.1016/j.cep.2017.09.005

[28] Zhang W, Xie P, Li Y, Teng L, Zhu J. 3D CFD simulation of the liquid flow in a rotating packed bed with structured wire mesh packing. *Chemical Engineering Journal*. 2022;427:130874. doi:10.1016/j.cej.2021.130874

[29] Guo TY, Shi X, Chu GW, Xiang Y, Wen LX, Chen JF. Computational Fluid Dynamics Analysis of the Micromixing Efficiency in a Rotating-Packed-Bed Reactor. *Ind Eng Chem Res*. 2016;55(17):4856-4866. doi:10.1021/acs.iecr.6b00213

[30] Yang Y, Xiang Y, Chu G, et al. CFD modeling of gas–liquid mass transfer process in a rotating packed bed. *Chemical Engineering Journal*. 2016;294:111-121. doi:10.1016/j.cej.2016.02.054

[31] Xie P, Lu X, Ingham D, Ma L, Pourkashanian M. Mass transfer characteristics of the liquid film flow in a rotating packed bed for CO2 capture: A micro-scale CFD analysis. *Energy Procedia*. 2017;142:3407-3414. doi:10.1016/j.egypro.2017.12.478

[32] Lu X, Xie P, Ingham DB, Ma L, Pourkashanian M. Modelling of CO2 absorption in a rotating packed bed using an Eulerian porous media approach. *Chemical Engineering Science*. 2019;199:302-318. doi:10.1016/j.ces.2019.01.029

[33] Zhang G, Ingham D, Ma L, Pourkashanian M. Modelling of 3D liquid dispersion in a rotating packed bed using an Eulerian porous medium approach. *Chemical Engineering Science*. 2022;250:117393. doi:10.1016/j.ces.2021.117393

[34] Lu X, Xie P, Ingham DB, Ma L, Pourkashanian M. A porous media model for CFD simulations of gas-liquid two-phase flow in rotating packed beds. *Chemical Engineering Science*. 2018;189:123-134. doi:10.1016/j.ces.2018.04.074

[35] Li YB, Wen ZN, Sun BC, Luo Y, Gao KJ, Chu GW. Flow patterns, liquid holdup, and wetting behavior of viscous liquids in a disk-distributor rotating packed bed. *Chemical Engineering Science*. 2022;252:117256. doi:10.1016/j.ces.2021.117256

[36] Chen S, Ouyang Y, Vandewalle LA, Heynderickx GJ, Van Geem KM. CFD analysis on hydrodynamics and residence time distribution in a gas-liquid vortex unit. *Chemical Engineering Journal*. 2022;446:136812. doi:10.1016/j.cej.2022.136812

[37] Zhang W, Xie P, Li Y, Zhu J. Modeling of gas–liquid flow in a rotating packed bed using an Eulerian multi-fluid approach. *AIChE Journal*. 2022;68(4). doi:10.1002/aic.17561

[38] Attou A, Boyer C, Ferschneider G. Modelling of the hydrodynamics of the cocurrent gas–liquid trickle flow through a trickle-bed reactor. *Chemical Engineering Science*. 1999;54(6):785-802. doi:10.1016/S0009-2509(98)00285-1

[39] Lappalainen K, Alopaeus V, Manninen M, Aittamaa J. Improved Hydrodynamic Model for Wetting Efficiency, Pressure Drop, and Liquid Holdup in Trickle-Bed Reactors. *Ind Eng Chem Res*. 2008;47(21):8436-8444. doi:10.1021/ie8003754

[40] Iliuta I, Petre CF, Larachi F. Hydrodynamic continuum model for two-phase flow structured-packing-containing columns. *Chemical Engineering Science*. 2004;59(4):879-888. doi:10.1016/j.ces.2003.11.020

[41] Kołodziej A, Łojewska J. Experimental and modelling study on flow resistance of wire gauzes. *Chemical Engineering and Processing: Process Intensification*. 2009;48(3):816-822. doi:10.1016/j.cep.2008.10.009

[42] Kołodziej A, Łojewska J, Jaroszyński M, Gancarczyk A, Jodłowski P. Heat transfer and flow resistance for stacked wire gauzes: Experiments and modelling. *International Journal of Heat and Fluid Flow*. 2012;33(1):101-108. doi:10.1016/j.ijheatfluidflow.2011.11.006

[43] Bussière W, Rochette D, Clain S, André P, Renard JB. Pressure drop measurements for woven metal mesh screens used in

electrical safety switchgears. *International Journal of Heat and Fluid Flow*. 2017;65:60-72. doi:10.1016/j.ijheatfluidflow.2017.02.008

[44] Lashkarbolooki M. A general model for pressure drop prediction across a rotating packed bed. *Separation Science and Technology*. 2017;52(11):1843-1851. doi:10.1080/01496395.2017.1302476

[45] Xie P, Lu X, Ding H, et al. A mesoscale 3D CFD analysis of the liquid flow in a rotating packed bed. *Chemical Engineering Science*. 2019;199:528-545. doi:10.1016/j.ces.2019.01.038

[46] Yang W, Wang Y, Chen J, Fei W. Computational fluid dynamic simulation of fluid flow in a rotating packed bed. *Chemical Engineering Journal*. 2010;156(3):582-587. doi:10.1016/j.cej.2009.04.013